Software Contribution

GEOSPHERE

GEOSPHERE, v. 17, no. 4

https://doi.org/10.1130/GES02259.1

12 figures; 2 tables

CORRESPONDENCE: cpscott1@asu.edu

CITATION: Scott, C., Phan, M., Nandigam, V., Crosby, C., and Arrowsmith, J R., 2021, Measuring change at Earth's surface: On-demand vertical and three-dimensional topographic differencing implemented in OpenTopography: Geosphere, v. 17, no. 4, p. 1318–1332, https://doi.org/10.1130/GES02259.1.

Science Editor: Andrea Hampel
Associate Editor: Brian J. Yanites

Received 17 March 2020
Revision received 16 October 2020
Accepted 1 March 2021

Published online 14 May 2021

Measuring change at Earth's surface: On-demand vertical and three-dimensional topographic differencing implemented in OpenTopography

Chelsea Scott[1], Minh Phan[2], Viswanath Nandigam[2], Christopher Crosby[3], and J Ramon Arrowsmith[1]

[1]School of Earth and Space Exploration, Arizona State University, Tempe, Arizona 85287, *USA*
[2]San Diego Supercomputer Center, University of California San Diego, La Jolla, California 92093, USA
[3]UNAVCO, Boulder, Colorado 80301, USA

ABSTRACT

Topographic differencing measures landscape change by comparing multitemporal high-resolution topography data sets. Here, we focused on two types of topographic differencing: (1) Vertical differencing is the subtraction of digital elevation models (DEMs) that span an event of interest. (2) Three-dimensional (3-D) differencing measures surface change by registering point clouds with a rigid deformation. We recently released topographic differencing in OpenTopography where users perform on-demand vertical and 3-D differencing via an online interface. OpenTopography is a U.S. National Science Foundation–funded facility that provides access to topographic data and processing tools. While topographic differencing has been applied in numerous research studies, the lack of standardization, particularly of 3-D differencing, requires the customization of processing for individual data sets and hinders the community's ability to efficiently perform differencing on the growing archive of topography data. Our paper focuses on streamlined techniques with which to efficiently difference data sets with varying spatial resolution and sensor type (i.e., optical vs. light detection and ranging [lidar]) and over variable landscapes. To optimize on-demand differencing, we considered algorithm choice and displacement resolution. The optimal resolution is controlled by point density, landscape characteristics (e.g., leaf-on vs. leaf-off), and data set quality. We provide processing options derived from metadata that allow users to produce optimal high-quality results, while experienced users can fine tune the parameters to suit their needs. We anticipate that the differencing tool will expand access to this state-of-the-art technology, will be a valuable educational tool, and will serve as a template for differencing the growing number of multitemporal topography data sets.

Chelsea Scott https://orcid.org/0000-0002-3884-4693

INTRODUCTION

Topographic differencing measures landscape change from urban growth, flooding (Wheaton et al., 2009; Izumida et al., 2017), coastal processes (Brock et al., 2001; Bull et al., 2010), earthquakes and creeping faults (Oskin et al., 2012; Nissen et al., 2012, 2014; Clark et al., 2017; Scott et al., 2018a; Wedmore et al., 2019; Barnhart et al., 2019; Scott et al., 2020), volcanic eruptions (Albino et al., 2015), and landslides (Lucieer et al., 2014), among other events. Interest in this technique is growing as more regions are surveyed with multitemporal topography data. Vertical differencing is the subtraction of raster-based digital elevation models (DEMs) and can be performed on original raster topography or grids generated from point cloud data, as shown in Figure 1. Three-dimensional (3-D) differencing resolves the best rigid deformation during an event of interest and is performed with a windowed implementation of the iterative closest point (ICP) algorithm (Besl and McKay, 1992; Chen and Medioni, 1992), as illustrated in Figure 2.

The 3-D differencing method, in particular, often requires an expert to dedicate substantial effort to customize processing, and there is little standard methodology or documentation available. As multitemporal topography coverage increases, more data types with variable characteristics are differenced, and results are used to respond to natural disasters and study phenomena altering Earth's surface. In this paper, we describe our implementation of on-demand vertical and 3-D differencing on topography data available via OpenTopography (opentopography.org). A major challenge in 3-D differencing is to select the appropriate differencing algorithm and the resolution of derived displacements, which depend on data resolution, noise, and landscape characteristics. We compared several differencing algorithms and incorporated metadata (e.g., point density) into the default processing settings. Our workflow quickly produces quality differencing results and offers default options that can be further tailored for individual data sets by more advanced users. Deployment of these tools in OpenTopography expands access to state-of-the-art technology for scientists, geospatial professionals, and students. Additionally, our tools can become a reference that contributes to the standardization of topographic differencing, which is lacking in the geosciences.

OpenTopography is a U.S. National Science Foundation–funded facility that enables discovery and access of high-resolution topography data sets and provides on-demand processing tools. OpenTopography is built on a scalable-system–oriented architecture that supports a range of downstream processing tools that derive common science products from hosted raw data (Krishnan et al., 2011). As of October 2020, the 341 point cloud data sets hosted by OpenTopography cover more than

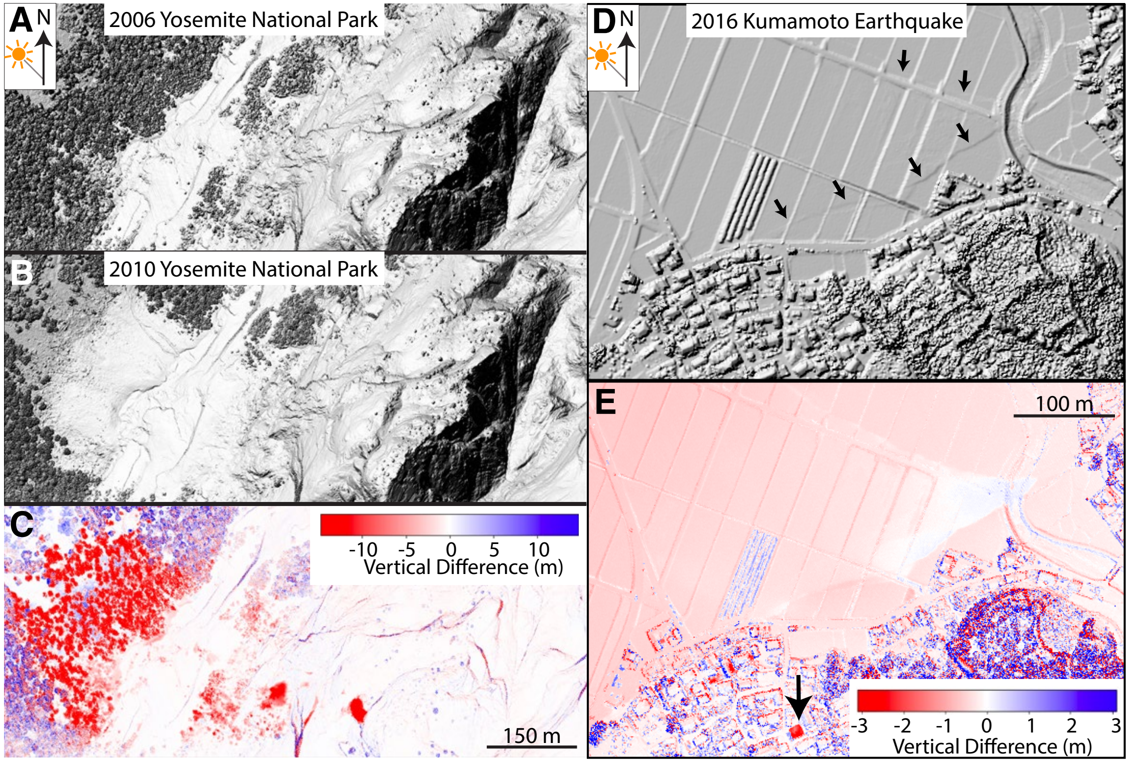

Figure 1. Vertical differencing in OpenTopography. (A–B) Topographic hillshades of Yosemite National Park, California (37° 45.175′N, 119° 32.509′W), from airborne light detection and ranging (lidar) data acquired in 2006 (A) and 2010 (B). (C) Differencing shows rockfalls and treefalls near cliff edges (red) and vegetation changes (purple). (D) Tectonic fault (black arrows) ruptures through agricultural fields during the M 7 2016 Kumamoto, Japan (32° 47.788′N, 130° 51.099′E), earthquake. (E) Topographic differencing: Downward motion (red) is punctuated by two faults that produce sharp displacement changes. Red square represents a collapsed building. Hillshade illumination is from the northwest. Outputs were generated directly via the OpenTopography workflow. Yosemite lidar: 2006 (Stock, 2012) and 2010 (Zimmer, 2011); Kumamoto lidar: (Chiba, 2018b, 2018a).

266,000 km^2 with over 1.6 trillion returns. Since its founding in 2009, almost 500,000 point cloud and raster jobs have been run via the portal, with an additional 1 million jobs run via the available application programming interface. The processing tools are designed to be accessible to users with a range of geospatial knowledge and experience, from beginners to geospatial professionals, including students, environmental engineers, urban planners, and geologists. To accommodate the diverse user community, novice users are guided by interactive interfaces where processing algorithms are prepopulated with optimal parameters for best results. Advanced users can change the default options in the available algorithms to tailor the analysis according to their needs. In on-demand differencing via the portal, users select overlapping data sets for differencing and can process the data with the suggested default parameters (e.g., spatial resolution) or customize the processing.

In the next section, we review established methodology on general topographic differencing, topography data sets and error, DEM generation, and vertical and 3-D differencing. We then describe our vertical differencing implementation in OpenTopography using primarily open-source software with an emphasis on data set resolution and error. Subsequently, we address several challenges in standardizing 3-D differencing, including selecting the right differencing algorithm and optimizing the spatial resolution given modern and legacy data sets in different landscape types. We show that the optimal spatial resolution (i.e., window size) depends on point density, data set quality, and vegetation characteristics. We detail the implementation of 3-D on-demand differencing in the portal. Last, we summarize lessons learned on topographic differencing, differencing algorithm usage, and remaining challenges.

BACKGROUND

Overview of Differencing Approaches

Surface change detection from multitemporal topographic data sets reveals landscape change. Typically, the differenced data sets are acquired for dissimilar purposes and with varying technology, resolution, and precision (Fig. 3). A differencing algorithm that can ingest diverse data types is therefore more widely applicable.

There are multiple approaches for calculating surface change from topography data acquired

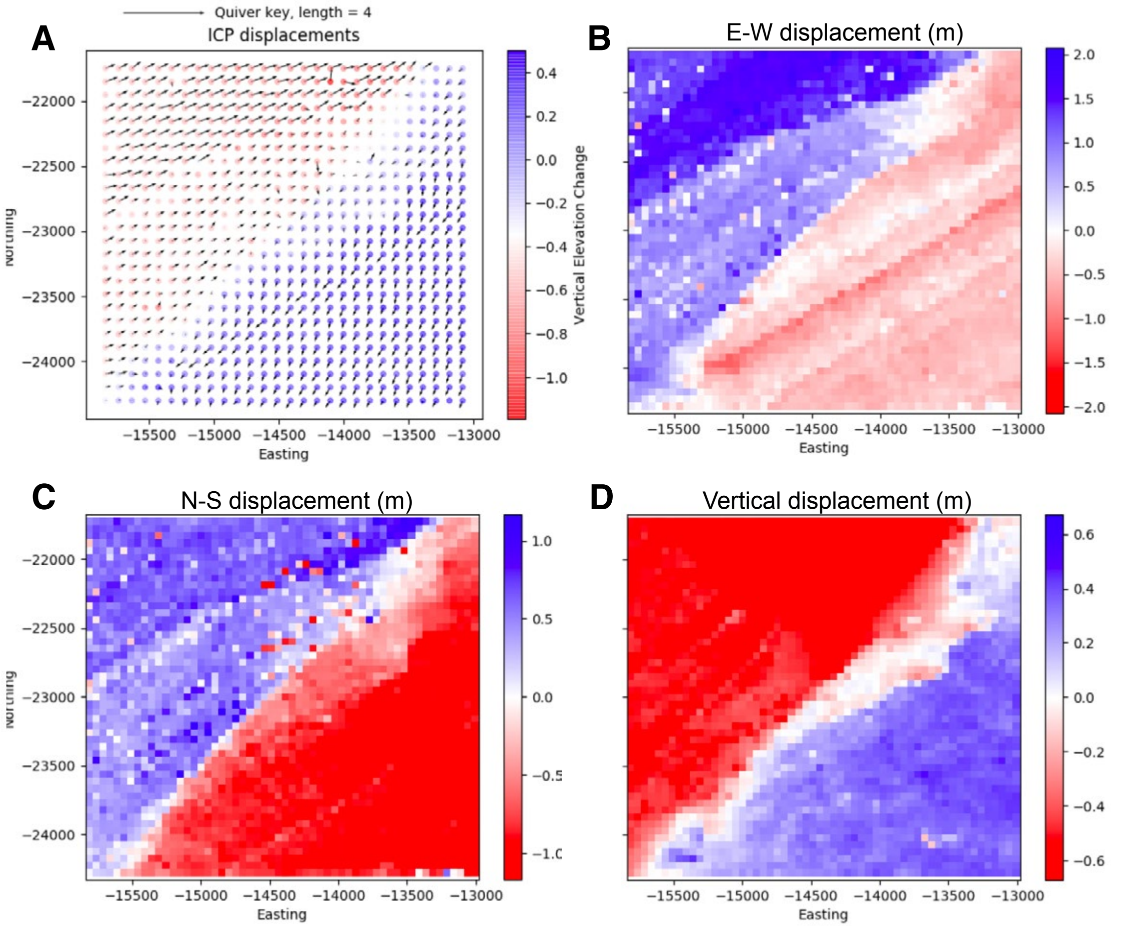

Figure 2. Three-dimensional (3-D) iterative closest point (ICP) algorithm differencing for the 2016 M 7 Kumamoto, Japan, earthquake performed on OpenTopography. (A) 3-D displacement field: Arrows and filled circles represent the horizontal and vertical displacement, respectively. (B) East-west, (C) north-south, and (D) vertical displacement. The earthquake produced ~2 m of oblique right-lateral surface slip. Outputs were generated directly via the OpenTopography workflow. Data sets: Chiba (2018a, 2018b).

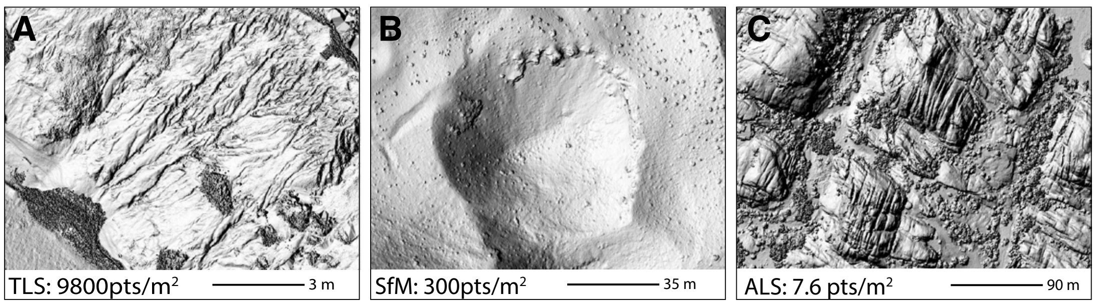

Figure 3. High-resolution topographic hillshades: (A) Terrestrial laser scanning (TLS) along a coastal bluff in Solano Beach, California (32° 59.425′N, 117° 16.472′W; SDRCC, 2018). (B) Structure-from-motion (SfM) topography from a small uncrewed aerial system (sUAS) showing a conical vent along the Tecolote Volcano, Sonora, Mexico (31° 52.682′N, 113° 21.760′W; Scott et al., 2018b). (C) Airborne laser scanning (ALS) showing fractured rocks in the Granite Dells, Arizona (34° 36.124′N, 112° 25.316′W; Haddad, 2010).

from terrestrial, airborne, and space-based platforms. Vertical differencing (Fig. 1) is the raster subtraction of two DEMs, and it can capture geologic processes including river erosion, flooding (Wheaton et al., 2009; Izumida et al., 2017), earthquakes (Oskin et al., 2012; Clark et al., 2017), volcanic eruptions (Albino et al., 2015), and landslides (Lucieer et al., 2014). Vertical differencing works well in flat areas or when the surface change is dominantly vertical, but lateral shifts due to coseismic offset result in topographically correlated artifacts when the data sets are no longer coregistered (e.g., Oskin et al., 2012). However, the relative offset between topographic data sets may be used to solve for horizontal motion (Streutker et al., 2011; DeLong et al., 2012; Donnellan et al., 2017). Cross-correlation algorithms applied to topographic hillshades, optical, and radar data sets quantify horizontal displacement (Leprince et al., 2007; Borsa and Minster, 2012; Milliner et al., 2015).

Other differencing approaches directly use point clouds. The cloud-to-cloud distance tool in CloudCompare (cloudcompare.org) measures local point cloud separation. The Multiscale Model to Model Cloud Comparison (M3C2; Lague et al., 2013) calculates cloud-to-cloud separation in the surface-normal direction and has been applied to bank and bedrock erosion and prograding deltas (Wagner et al., 2017; Beer et al., 2017; Leyland et al., 2017). A windowed implementation of the ICP algorithm (Besl and McKay, 1992; Chen and Medioni, 1992) solves for the rigid-body 3-D deformation by registering subsets of pre- and postevent topography.

The data set acquired before the event of interest is called the "pre," "compare," or "source" data set. The data set acquired after the event is the "post," "reference," or "target" data set. The compare and reference terminology is more commonly used in the vertical differencing literature (Wheaton et al., 2009), while source and target are used for 3-D differencing (Nissen et al., 2012). We use compare and reference terms for both vertical and 3-D differencing for consistency.

Topography and Error

Topographic data derived from laser- and photogrammetry-based techniques are often presented as a point cloud (Fig. 4). The spatial sampling may vary by several orders of magnitude depending on the sensor type (e.g., terrestrial vs. airborne laser scanning; Fig. 3) and the available technology. A DEM is generated by rasterizing the point cloud to a horizontal grid.

Because topographic differencing quantifies relatively small changes between topography data sets, survey and metadata errors often become pronounced. Due to rapid advances in light detection and ranging (lidar) scanning systems, the older compare data set often has the larger error. Typical airborne lidar point clouds have vertical errors of 5–15 cm when the flight altitude is below 1200 m due to inertial measurement unit, boresight, laser, scanner, lever arm offset, incidence angle, and differential global navigation satellite system (dGNSS) kinematic position errors (Toth et al., 2007; Glennie, 2007; Goulden and Hopkinson, 2010). Horizontal errors are often five times larger than vertical errors. Metadata often include no error or only a single error that represents a flat and unvegetated surface. Errors are larger over high-relief landscapes due to range-finder errors caused by changes in scanning geometry (Schaer et al., 2007). Light detection and ranging surveys typically consist of data acquired along multiple paths or flight lines. Flight-line offset often creates linear artifacts in differencing results (Fig. 2) aligned with the flight direction. Resolution or point density depends on flight design and sensor properties. Typical airborne lidar point density has increased over time, from ~0.1–2 points/m^2 for data acquired before 2007 (termed legacy data) to ~1–30 points/m^2 for modern data (Passalacqua et al., 2015; Okyay et al., 2019). Because differencing requires that both data sets are in identical coordinate systems, good metadata are critical for mitigating coregistration errors. Point classification adds additional error, ranging from minimal over bare earth to the vegetation height when features cannot be removed (e.g., Passalacqua et al., 2015).

Photogrammetric point clouds produced from small uncrewed aerial system (sUAS) optical imagery and structure-from-motion (SfM) techniques have errors due to onboard navigation systems with multimeter accuracy and doming due to radial lens distortion (James and Robson, 2014). External ground-control points measured with dGNSS translate, orient, and scale the point cloud. Position error correlates with the square root of the

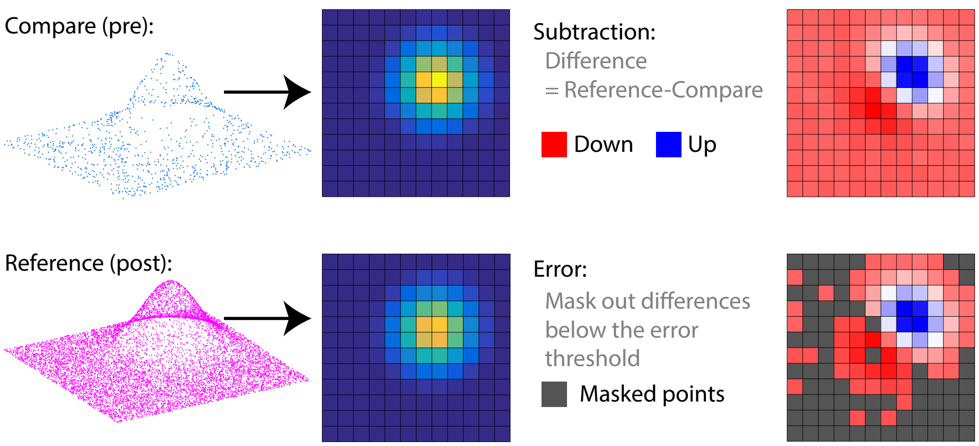

Figure 4. Vertical differencing: Compare (pre-event; blue) and reference (postevent; pink) point clouds with varying spatial resolution are gridded to identical rasters. Raster differencing reveals elevation changes: Red is downward change or erosion, and blue is upward change or deposition. Elevation changes below the error threshold are masked (gray).

number of ground-control points (James et al., 2017). DEMs generated from stereo-satellite imagery have decreased cost and increased spatial coverage in the last decade (e.g., Barnhart et al., 2019). DigitalGlobe DEMs have an ~2 m resolution with a <5 m geolocation accuracy that is reduced to 0.5 m with ground control (Shean et al., 2016). Both SfM- and stereo-satellite–derived topography methods record surface features, including vegetation (Anders et al., 2019). In contrast, lidar offers the ability to filter points returned from vegetation.

DEM Generation and Uncertainty

A DEM is a generic term for elevation values. A digital terrain model (DTM) refers to bare earth. A digital surface model (DSM) refers to the top of the landscape. DEMs are often produced from point clouds using local neighborhood, geostatistical, and spline methods (e.g., Passalacqua et al., 2015). The triangular irregular network (TIN) is a local neighborhood algorithm wherein the surface is represented by neighboring triangles. A Delauney triangulation creates nearly equilateral triangles. Inverse distance weighted (IDW) and inverse distance power (IDP) approaches calculate elevations along grid cells based on an inverse weighting of elevations given the Euclidean distance between the grid cell and data points, sometimes to a power. IDW/IDP methods result in few artifacts near holes commonly present in terrestrial laser scanning (TLS) data. The DEM spatial resolution is typically dictated by the point cloud resolution (e.g., Smith et al., 2019). DEM uncertainties represent grid resolution, terrain variability, and acquisition and processing errors (e.g., Smith et al., 2019).

Vertical Raster-Based Differencing

Vertical or raster-based differencing is performed on two DEMs in the same coordinate system and rasterized to identical grids. The differencing results in Figure 1 show rockfalls in Yosemite, California, and vertical displacements due to an earthquake in Japan. When point cloud and/or DEM errors are known, error propagation provides the differencing uncertainty (Wheaton et al., 2009). Differences below a minimum level of detection (E_{MLOD}) are usually masked. For a DEM vertical uncertainty of ∂z, the differencing uncertainty is (e.g., Brasington et al., 2003):

$$E_{MLOD} = \sqrt{\partial z_{reference}{}^{2} + \partial z_{compare}{}^{2}}. \qquad (1)$$

This equation requires that DEM errors are random and independent of landscape type (e.g., wet vs. dry and varying relief). Because DEM error is typically more complex, Equation 1 should be used if the signal is significantly larger than the error. We use Equation 1 in OpenTopography's error calculation.

3-D Differencing

The ICP algorithm used for 3-D differencing originated in the medical, robotics, and computer vision communities for registering 3-D scans (e.g., Bellekens et al., 2014; Besl and McKay, 1992). In the earth sciences, 3-D differencing is best applied to events where the landscape shifts laterally, like earthquakes and creeping landslides. As a proof-of-concept, Nissen et al. (2012) applied this approach to synthetically offset B4 airborne lidar data (Bevis et al., 2005) that mimic a surface-rupturing earthquake along the San Andreas fault, California. The method has since been applied to real earthquakes using airborne lidar (Clark et al., 2017; Nissen et al., 2012, 2014; Scott et al., 2018a, 2019), TLS (Wedmore et al., 2019), satellite optical (Barnhart et al., 2019), aerial photographs (Howell et al., 2020), and hybrid data sets (Ekhtari and Glennie, 2017; Scott et al., 2020).

In windowed 3-D differencing, surface change is calculated as the best rigid transformation (features translate and rotate while maintaining their shape and scale) that registers reference and compare windows of topography. For airborne laser scanning, the window size (i.e., resolution) is a few tens of meters. The rigid deformation is associated with a core point (Fig. 5; black dot) at the window center. Typically, there is no exact point-to-point match between the two point clouds due to noise, varying point density, and the fact that the same points are rarely resurveyed. The optimal window size is a trade-off between a large scale with greater topographic structure to produce a robust alignment and a small scale that is less likely to violate the rigid-body assumption (Nissen et al., 2012). In the "Window Size and Point Density" section, we show that point density, data quality, and vegetation control window size.

Scott et al. (2018a) used correlation error to assess uncertainty in airborne lidar ICP displacements. This error measures the local variability in displacements over ~100 × 100 m² areas. The

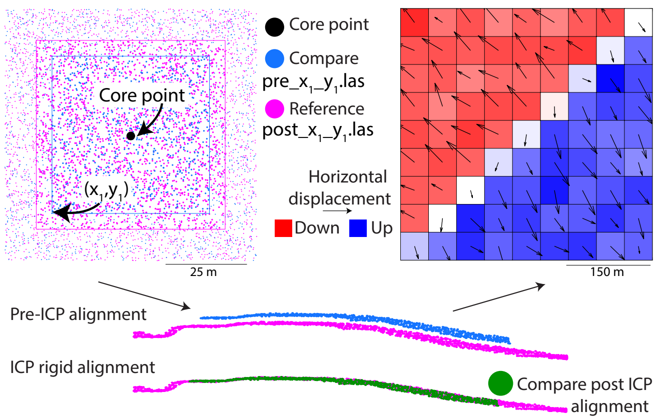

Figure 5. Three-dimensional (3-D) differencing of windowed point cloud topography. The compare (pre-event; blue) and reference (postevent; pink) data sets are delineated by windows (square outlines) around a core point (black dot). The reference data set has an additional buffer. Typically, the reference data set has a higher point density due to technology advancements over time. The point clouds are registered by a rigid deformation (translation and rotation) using the iterative closest point (ICP) algorithm. Applying the algorithm to a repeat survey results in a 3-D displacement field.

horizontal correlation error scaled inversely with topographic relief: In that study, the lower- and higher-relief landscapes had horizontal errors of 5–12 cm and 4–6 cm, respectively, while the 1–3 cm vertical errors had no relationship to land use.

VERTICAL DIFFERENCING IMPLEMENTATION IN OPENTOPOGRAPHY

To use the vertical differencing tool implemented in OpenTopography, a user selects a data set pair from a subset of overlapping data sets with identical coordinate systems, as shown in Figure 6. The user is presented with differencing options: (1) The reference and compare data sets can be switched, ultimately impacting the differencing product sign (e.g., if erosion or deposition is negative). (2) When both data sets have been classified, differencing can be performed with a subset of the classifications (i.e., ground-classified points) or on the DTM or DSM. (3) The optimal grid resolution (*GR*) of the differencing product is obtained when the lower-resolution data set point density is less than 1 pt/m², so the recommended *GR* is (e.g., Hu, 2003; Langridge et al., 2014):

$$GR = \frac{1}{\sqrt{point\ density}}. \quad (2)$$

When the point density exceeds 1 pt/m², the 1 m default resolution increases processing speeds. The user can alter the resolution, but gridding too finely may result in artifacts.

Differencing can be performed starting with point cloud or raster topography. Both data types are rasterized to identical grids (origin, boundaries, and resolution). Point cloud data sets are gridded to a DEM using the TIN algorithm. The raster data sets are regridded using the Geospatial Data Abstraction Library (GDAL/OGR contributors, 2019): Gdalwarp crops the data set to the appropriate bounds, and gdal_translate grids the data set to appropriate resolution. To produce the differencing result (z_{Diff}), the reference ($z_{reference}$) and compare ($z_{compare}$) DEMs are subtracted using gdal_calc:

$$z_{Diff} = z_{reference} - z_{compare}. \quad (3)$$

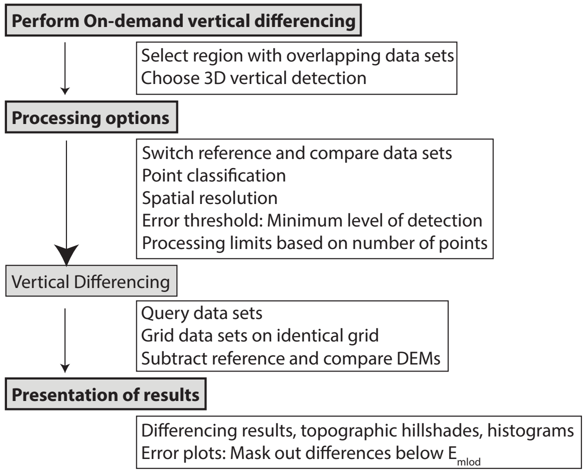

Figure 6. Flow chart for vertical differencing implemented in OpenTopography. Bolded text denotes areas of user interaction. Nonbolded text requires no user interaction. DEMs—digital elevation models; E_{MLOD}—error threshold for minimum level of detection.

When $z_{reference}$ was acquired after $z_{compare}$ (the default setting), positive and negative z_{Diff} values denote upward and downward change, respectively. The suggested E_{MLOD} = 0.5 m corresponds to ∂z = 0.35 m for both DEMs. While conservative for current lidar surveys, the range is likely intuitive for many users. Users can alter the E_{MLOD} value, rerun the differencing, and assess the most representative error. Because metadata do not typically include error, the E_{MLOD} suggestions do not reflect an individual data set. Using this method, we generated the following outputs: (1) DEM topographic hillshades, (2) z_{diff} values, and (3) a z_{diff} histogram (Fig. 7). With the selected error option, we display (4) z_{diff} values and (5) a histogram with differences below the threshold masked. These products can be downloaded from the OpenTopography results page for that job.

3-D DIFFERENCING ALGORITHM DEVELOPMENT AND IMPLEMENTATION

Differencing Algorithms

There are several variations of the 3-D differencing algorithm. The common ICP point-to-point algorithm aligns point clouds based on the correspondence between nearest neighbors, which is preferable when surfaces are quadratic or polynomial (Bellekens et al., 2014). The ICP point-to-plane algorithm aligns compare points with the reference plane. The algorithm penalizes for separation in the surface-normal direction but not for horizontal misalignments across flat topography. It is less sensitive to noise when topography is approximately planar and is advantageous when an exact point match is unlikely, such as when the point density varies between data sets. The ICP nonlinear method uses the point-to-point and point-to-plane approaches for global and fine alignment, respectively (e.g., Bellekens et al., 2014). Other approaches also use color (e.g., Men et al., 2011) or solve for scale (Amberg et al., 2007).

To calculate 3-D displacements, the point cloud data set delineated into windows (Fig. 5). A buffer exceeding the plausible horizontal displacement and rotation is added to the reference data set so that the transformed compare ($PC_{compare}^{transformed}$) and original reference point clouds ($PC_{reference}$) align. After applying the best 3-D rigid body deformation to the compare point cloud ($PC_{compare}$), $PC_{compare}^{transformed}$ and $PC_{reference}$ align:

$$PC_{compare}^{transformed} = \begin{pmatrix} 1 & -\gamma & \beta \\ \gamma & 1 & -\alpha \\ -\beta & \alpha & 1 \end{pmatrix} PC_{compare} + \begin{pmatrix} t_x \\ t_y \\ t_z \end{pmatrix}. \quad (4)$$

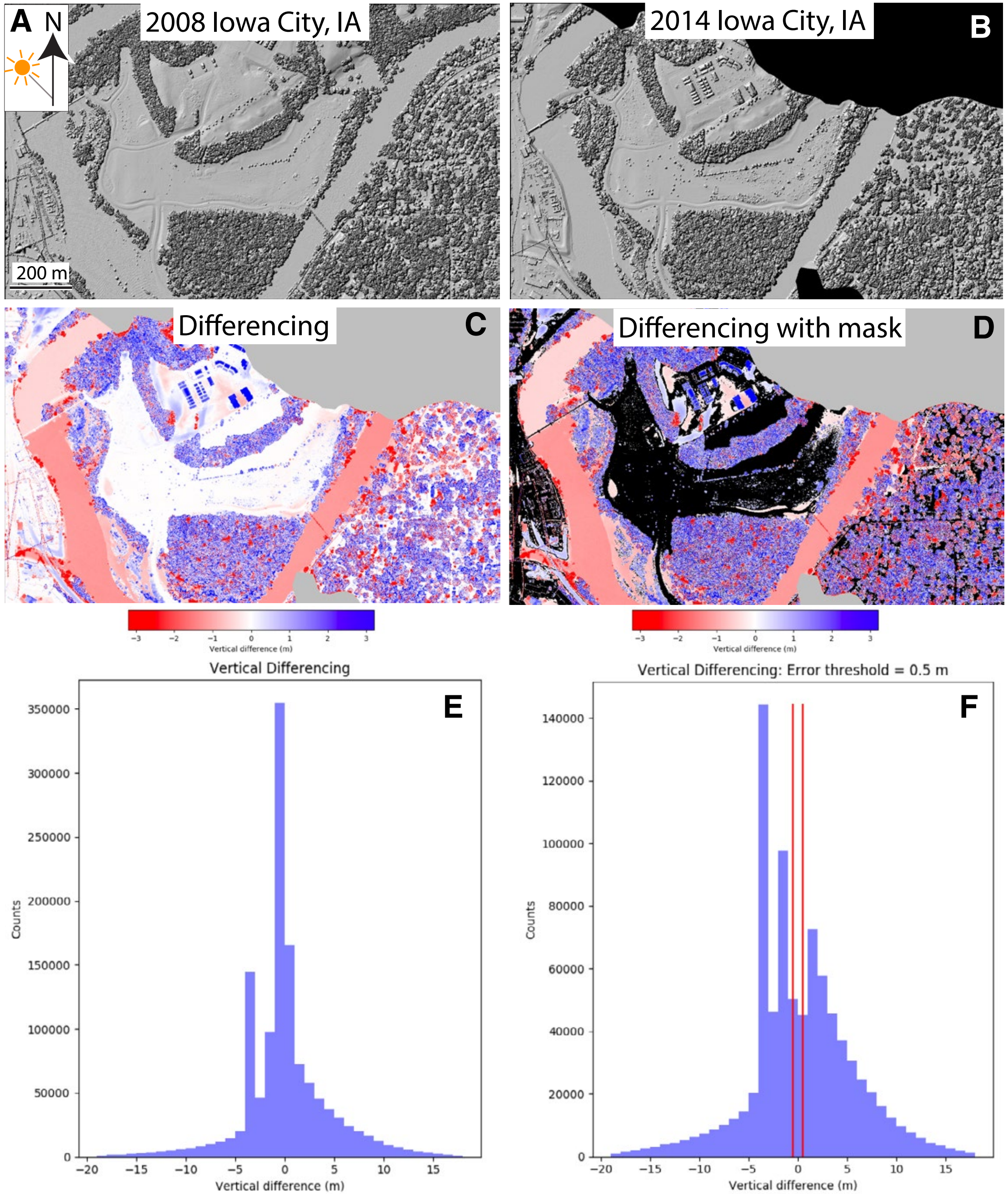

Figure 7. (A–B) Vertical differencing results in Iowa City, Iowa, from 2008 (A) to 2014 (B) generated via OpenTopography. (C) Differencing results highlight a drop in river level (red), building construction (blue), and vegetation changes (purple). (D) Displacements below a 0.5 m error threshold are masked (black). (E) Vertical differencing histogram. (F) Histogram with E_{MLOD} = 0.5 m (red bars). Data sets: 2008 (Krajewski, 2012); 2014 (Kumar, 2016). Location is 41° 40.361′N, 91° 33.490′W.

Here, α, β, and γ are rotations about the x, y, and z axes, and t_x, t_y, and t_z are translations in the x, y, and z directions. Equation 4 is written succinctly as

$$PC_{pre}^{transformed} = \varphi PC_{pre}, \tag{5}$$

where φ is the rigid transformation:

$$\varphi = \begin{pmatrix} 1 & -\gamma & \beta & t_x \\ \gamma & 1 & -\alpha & t_y \\ -\beta & \alpha & 1 & t_z \\ 0 & 0 & 0 & 1 \end{pmatrix}. \tag{6}$$

ICP approaches penalize misalignments and outlier treatments differently (Rusinkiewicz and Levoy, 2001). The point-to-point error (E_{p2p}) penalizes for misalignment between individual $PC_{compare}$ points and the nearest neighbor in $PC_{reference}$:

$$E_{p2p} = \sqrt{\sum_{i=1}^{Compare\ point\ cloud} \left|\left(\varphi PC_{compare,\,i} - PC_{reference,\,i}\right)\right|^2}. \tag{7}$$

The ICP point-to-plane error (E_{p2l}) is:

$$E_{p2l} = \sqrt{\sum_{i=1}^{Compare\ point\ cloud} \left|\left(\varphi PC_{compare,\,i} - PC_{reference,\,i}\right)\cdot n_i\right|^2}, \tag{8}$$

where n_i is the surface-normal vector at the ith point of $PC_{reference}$. When the net 3-D rotation is small (<30°), the problem can be linearized and solved with linear least squares (Low, 2004).

3-D Differencing Algorithm Choice

We compared two open-source ICP algorithms using airborne lidar topography for the 2016 M 7 Kumamoto, Japan, earthquake (Chiba, 2018a, 2018b; Scott et al., 2018a, 2019), as shown in Figure 8. The Library for ICP (LIBICP) was developed by Geiger et al. (2012) for 3-D object identification in autonomous navigation with point-to-point and point-to-plane implementation options. For the latter option, the normal vector is computed from

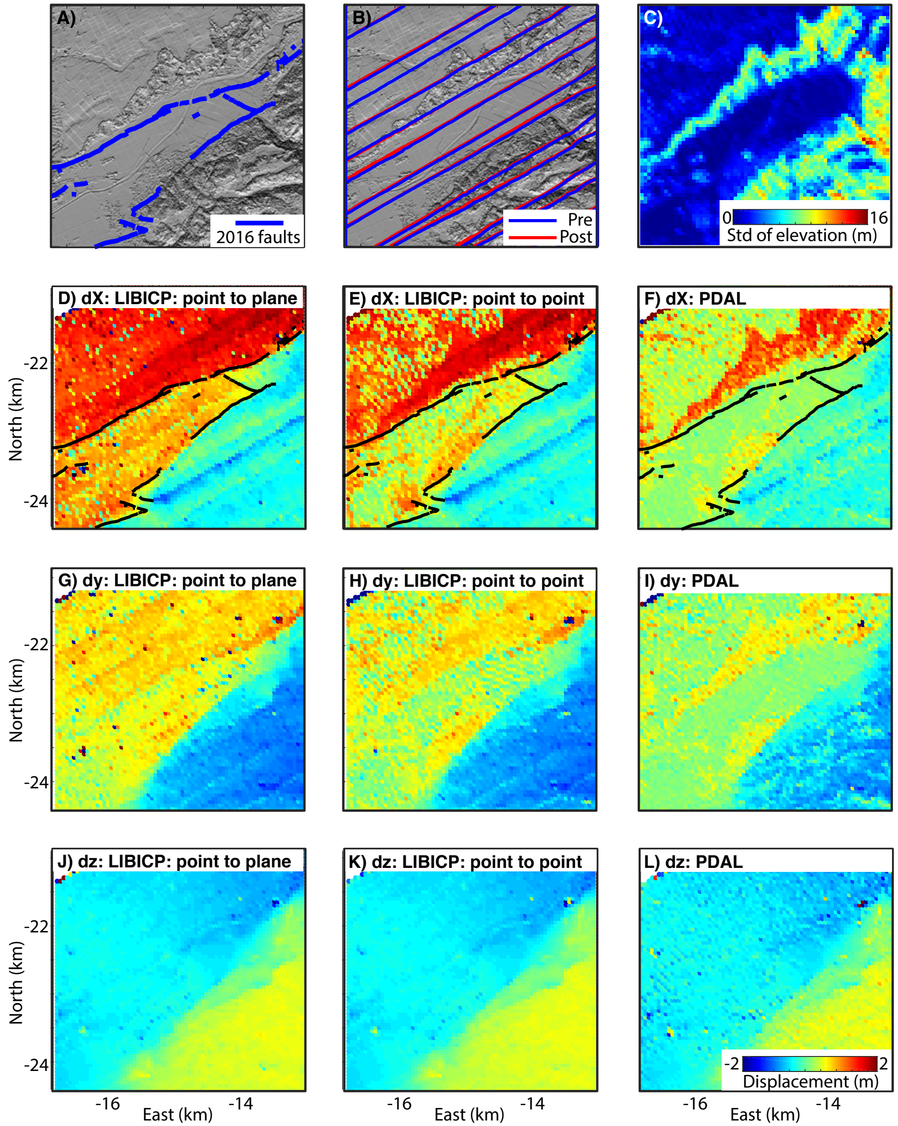

Figure 8. Three-dimensional (3-D) iterative closest point (ICP) algorithm displacements derived from three algorithms applied to the 2016 M 7 Kumamoto, Japan, earthquake light detection and ranging (lidar) topography (Chiba, 2018a, 2018b). Kumamoto Japan: 32° 47.788′N, 130° 51.099′E. (A) Topographic hillshade and fault ruptures mapped by the Japanese National Institute of Advanced Industrial Science and Technology (2016). (B) Pre-earthquake (blue) and post-earthquake (red) airborne lidar flight line boundaries. (C) Standard deviation of elevation over 50 × 50 m² windows. (D–F) Second row shows east-west displacement from the Library for ICP (LIBICP) point-to-plane (D), LIBICP point-to-point (E), and Point Data Abstraction Library (PDAL) (F) algorithms. (G–L) Third and fourth rows show north-south (G–I) and vertical displacements (J–L), respectively.

the default 10 nearest neighbors, which lie over ~1 m² for typical modern airborne lidar data. The second algorithm was the ICP filter in the Point Data Abstraction Library (PDAL; PDAL Contributors, 2018) point-to-point algorithm. We computed surface displacements using the three ICP implementations over 12 km² from 50 m windows and accessed quality from the correlation between displacements, fault ruptures, airborne lidar flight lines, and landscape. We expected variable ICP behavior over different landscape types and sharp displacement changes along faults. Displacement changes that correlate with flight-line boundaries (Fig. 8B) represent data-quality issues.

Horizontal displacements varied by algorithm and implementation (Fig. 8). The LIBICP point-to-plane displacements changed along faults and flight-line boundaries (Fig. 8D). Both point-to-point methods produced scattered displacements that correlated with land use (Figs. 8E and 8F), such as the agricultural-village boundary northwest of the fault. Vertical displacements that were estimated by aligning the point cloud vertical centroids were similar between methods. We prefer the LIBICP point-to-plane algorithm, which likely performs better because, locally, Earth's surface is approximately planar.

Window Size and Point Density

Topographic differencing algorithms ingest data sets with varying point density (Fig. 3), including legacy data that become invaluable following an event of interest (Oskin et al., 2012; Glennie et al., 2014), or conduct hybrid differencing that uses topography measured with different sensor types (Ekhtari and Glennie, 2017; Scott et al., 2020). We assessed the impact of point density on ICP window size from experiments that mimicked the study by Nissen et al. (2012), who synthetically offset airborne lidar data to explore ICP methodology. They separated lidar data into synthetic compare and reference topography data sets based on flight line, giving no exact point-to-point match between point clouds.

We conducted similar experiments on the data sets listed in Tables 1 and 2. We split each original data set in half using MATLAB's random number

TABLE 1. SAMPLE AIRBORNE LIGHT DETECTION AND RANGING (lidar) DATA SETS, WHERE THE MEAN HORIZONTAL ITERATIVE CLOSEST POINT (ICP) ERROR IS LESS THAN 20 CM ERROR THRESHOLD IN THE EXPERIMENT DESCRIBED IN "WINDOW SIZE AND POINT DENSITY" SECTION OF TEXT

Data set name	Date	Class	Point density (points/m²)
EarthScope, Northern California	March 2007	All	1.6–3.1
Missiquoi Watershed, Vermont	2008	All	0.7
Jemez, New Mexico, CZO Snow-on	March 2010	All	4.7
Jemez, New Mexico , CZO Snow-off	June 2010	All	1.7–5.2
Susquehanna, Pennsylvania, Shales Hill CZO Leaf-Off	April 2010	All	1.6–6.4
Susquehanna, Pennsylvania, Shales Hill CZO Leaf-On	July 2010	All	1.8–7.3
Apopka, Florida	2011	All	0.4–3.4
PG&E Diablo Canyon Power Plant: Los Osos, California	2011	All	0.3–5.4
Tahoe National Forest, California	2013	All	1.2–7.4
State of Utah: Wasatch Front	2013–2014	All	0.3–7.9
Wellington, New Zealand	2013	All	0.8–3.1
IML CZO, Clear Creek, Iowa	2014	All	0.5–4.1
Slumgullion Landslide, Colorado (July 3)	2015	All	0.6–9.0
EarthScope, Northern California	March 2007	Ground	1.4–2.1
Susquehanna, Pennsylvania, Shales Hill CZO Leaf-On	July 2010	Ground	0.1–0.5
El Mayor–Cucupah (EMC) earthquake	Aug 2010	Ground	0.7–4.0
Lunar Crater field, Nevada	June 2012	Ground	1.1–4.4
Tahoe National Forest, California	2013	Ground	0.1–0.5
State of Utah: Wasatch Front	2013–2014	Ground	0.3–2.5

Note: The point density range represents each of the synthetic compare and reference data sets. The lowest point density represents each half data set at the maximum thinning. OpenTopography hosts all data sets. CZO—critical zone observatory, IML—intensely managed landscape. Data set citations: EarthScope, Northern California (NCAL) (EarthScope, 2008; Prentice et al., 2009); Vermont (USGS, 2013); Jemez snow-off (Santa Catalina Mountains CZO, 2012a); Jemez snow-on (Santa Catalina Mountains CZO, 2012b); Susquehanna leaf-off (Susquehanna Shale Hills CZO, 2013a); Susquehanna leaf-on (Susquehanna Shale Hills CZO, 2013b); Florida (Catano, 2012); PG&E Diablo Canyon (DCPP LTSP, 2011); U.S. Forest Service (USFS, 2013); State of Utah (Utah, 2014); Wellington, New Zealand (GWRC, 2017); Iowa (Kumar, 2016); Slumgullion (Lee, 2017); El Mayor–Cucupah earthquake (Oskin et al., 2010); Lunar Crater volcanic field, Nevada (Valentine, 2012).

TABLE 2. SAMPLE AIRBORNE LIGHT DETECTION AND RANGING (lidar) DATA SETS, WHERE THE MEAN HORIZONTAL ITERATIVE CLOSEST POINT (ICP) ERROR EXCEEDS 20 CM FOR WINDOW SIZES LESS THAN 250 M BASED ON THE EXPERIMENT DESCRIBED IN "WINDOW SIZE AND POINT DENSITY" SECTION OF TEXT

Data set name	Date of acquisition	Point density (points/m²)
West Rainier seismic zone, Washington	2002	2.40
Idaho Lidar Consortium: Moscow Mountain	2003	0.35
San Diego Urban Region lidar	2005	1.41
Indiana statewide lidar	2011–2013	1.56
New Madrid seismic zone	2012	8.87

Note: Point density represents each of the synthetic compare and reference data sets. OpenTopography hosts all data sets. Rainier (NASA, 2005); Idaho (ILC, 2012); San Diego (City of San Diego, 2011); Indiana (IndianaMap, 2012); New Madrid (Williams and Weaver, 2012).

generator, resulting in sensitivity to point density and landscape type but losing sensitivity to spatially correlated Global Navigation Satellite System/Inertial Navigation System (GNSS/INS) trajectory and scanning geometry errors. Typically, the overlap between adjacent flight lines is insufficient to split by flight line. We shifted the entire post data set by 1 m eastward, 1 m southward, and 3 m upward. We estimated the 3-D displacement field using the LIBICP point-to-plane algorithm on 300 core points with variable spacing and a window size that increased in steps of 5 m to a maximum of 250 m. We calculated error from the root-mean-square difference between the input and estimated deformation. At the optimal window size, the mean horizontal error was equal to the 20 cm error threshold. We artificially thinned data sets to explore a broader range of point density.

Window size controlled displacement error for the 2013–2014 State of Utah Wasatch Front (7.9 points/m² point density; Utah, 2014) and the 2011–2013 Indiana data sets (0.6 points/m²; IndianaMap, 2012) as shown in Figure 9. For both data sets, horizontal errors exceeded vertical errors. For the Wasatch data set, a 25 m window size was below the 20 cm error threshold. The Indiana data set errors decayed with increasing window size but always exceeded the error threshold. The data sets in Table 1 produced mean horizontal errors less than the 20 cm threshold for the indicated window sizes, and those in Table 2 produced errors that exceeded 20 cm for window sizes below 250 m. We conducted the analyses using all points (Fig. 10A) and ground-classified points (Fig. 10B).

For the Wasatch (Utah, 2014), Los Osos (DCPP LTSP, 2013), Florida (Catano, 2012), Wellington (GWRC, 2017), Slumgullion (Lee, 2017), and Iowa (Kumar, 2016) data sets, the optimal window size increased with decreasing point density (Fig. 10). The varying leaf-on and leaf-off behavior suggests that landscape and season impact window size. The April 2010 leaf-off and the July 2010 leaf-on data sets in Susquehanna, Pennsylvania, had optimal window sizes of 35–50 m and 60–70 m, respectively (Susquehanna Shale Hills CZO, 2013a, 2013b). Likely, the leaf-off case is preferable due to the improved point cloud alignment in the absence of a tree canopy.

Using full airborne lidar data sets (Table 1; Fig. 10A), we fit an exponential decay relationship between the optimal window size (ws_{full}) and point density (pd):

$$ws_{\mathrm{full}} = 187\ e^{-2.26\ pd} + 45. \tag{9}$$

The optimal window was ~45 m when the point density exceeded 2 points/m², and larger window sizes were required for lower point density. Using ground-classified points, the optimal window size (ws_{ground}) was:

$$ws_{ground} = 233\ e^{-7.62\ pd} + 32. \tag{10}$$

Typically, ground-classified points have a lower point density than the full data set. Still, we found that a smaller window size is optimal when the ground-classified point density exceeds 0.5 points/m².

When the ground point density was less than 0.5 points/m², a larger window size was required, and so using the full point cloud would be advantageous, particularly over high vegetation.

In OpenTopography, we used the 95% confidence level (i.e., 2σ) upper bound of Equation 9 to recommend window size based on the lower-resolution data set's point density. Although conservative, this recommendation produces quality results for most data sets. Wedmore et al. (2019) preferred a 1 m window size for TLS data, showing that increasing resolution by a factor of 100 impacts window size. The larger errors (>20 cm) of data sets in Table 2 reflect lower point density and data quality. Because many of these were acquired before those in Table 1, the acquisition date serves as a secondary window size control.

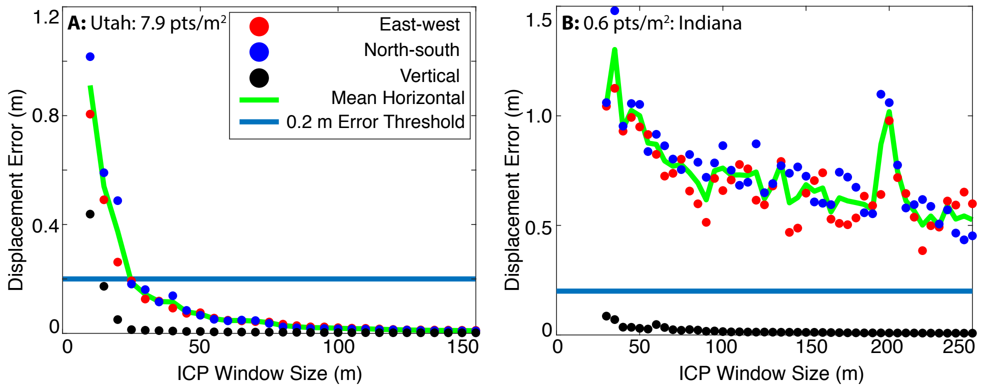

Figure 9. (A) Displacement error vs. window size for the 2013–2014 airborne light detection and ranging (lidar) State of Utah Wasatch Front data (Utah, 2014) with simulated pre- and postevent data, both with 7.9 points/m². The mean horizontal error (green line) is below the 20 cm horizontal error threshold at a 25 m window size. (B) Error for the 2011–2013 Indiana data set (IndianaMap, 2012) with 0.6 points/m². The mean horizontal error exceeds the error threshold. ICP—iterative closest point algorithm.

Window Size: Topographic Relief

We explored the impact of topographic relief on window size using the experiment described in the "Window Size and Point Density" section and the Wasatch data set (Utah, 2014), which spans the relatively flat urban Salt Lake City landscape and the higher-relief Wasatch Range (Fig. 11A). Topographic relief was measured as the standard deviation of elevation over 50 m windows. For the full data set (Fig. 11B), ICP error showed some dependence on topographic relief: Given the 20 cm error threshold, the lowest and highest relief areas required a 35 m window, while the middle-relief areas required a 20 m window. Low-relief areas had higher error due to the lower 3-D structure

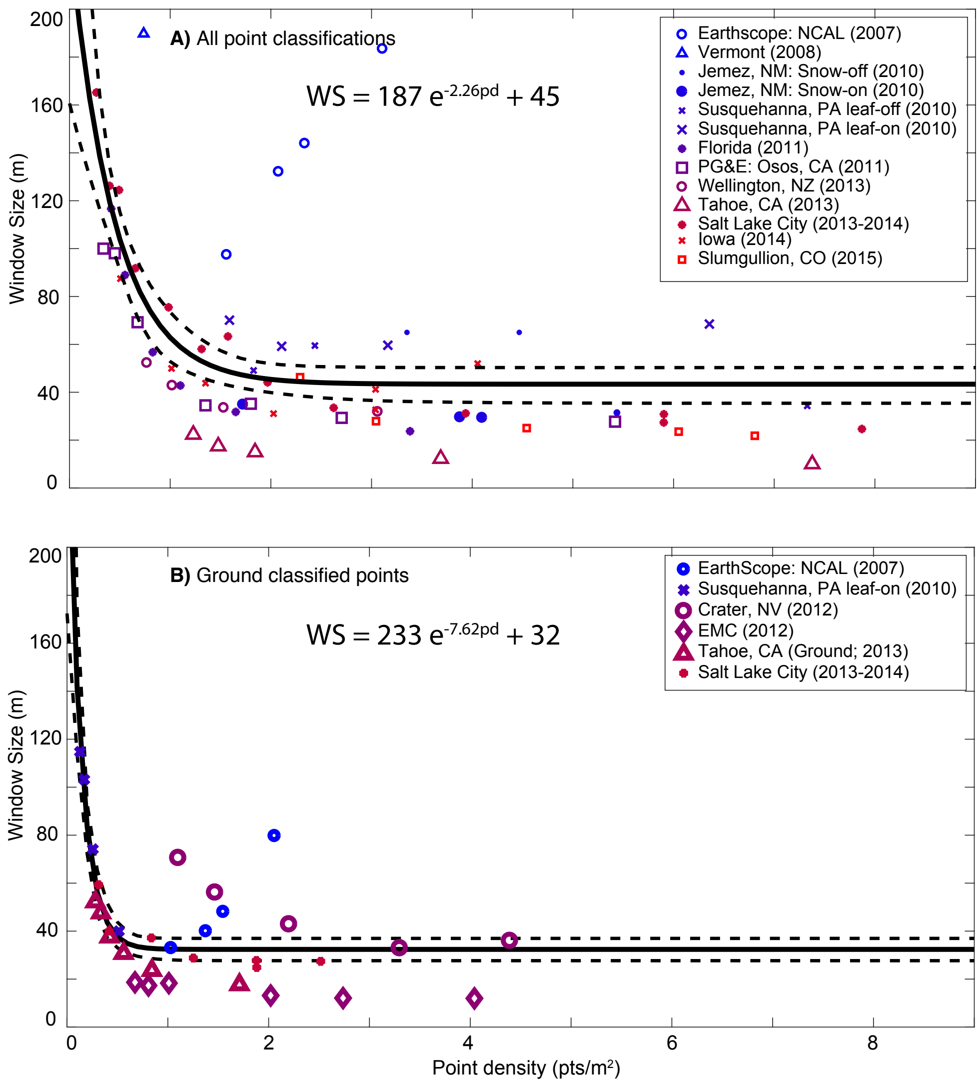

Figure 10. Optimal iterative closest point (ICP) algorithm window size (WS) vs. point density for synthetically offset airborne light detection and ranging (lidar) data sets given the 20 cm horizontal error threshold. Data sets are listed by acquisition year and cited in Table 1; Salt Lake City corresponds to State of Utah data in Table 1. Data sets plotted multiple times were artificially thinned. (A) All point classifications. (B) Ground-classified points. Solid lines—best-fit exponential curves (Eqs. 9 and 10); dashed lines—2σ error. NCAL—Northern California; NM—New Mexico; PA—Pennsylvania; CA—California; NZ—New Zealand; CO—Colorado; NV—Nevada; EMC—El Mayor–Cucupah.

available for alignment. The Wasatch mountains likely benefited from a larger window size due to the higher point cloud error and vegetation. Using only ground-characterized points (Fig. 11C), the preferred window size decreased, and the relief extremes no longer required the largest windows.

Implementation in OpenTopography

We used the insights described above to implement 3-D differencing in OpenTopography. Like vertical differencing, 3-D differencing is performed by differencing overlapping data sets in the same coordinate system (Fig. 12) with all or a subset of point cloud classifications. The recommended window size is the 2σ upper bound of Equation 9, based on the average point density of the entire data set stored in the metadata, although point density varies spatially. We used a licensed version of the LAStools software package (LAStile; Isenburg et al., 2006) for point cloud windowing and the LIBICP point-to-plane algorithm for differencing (Geiger et al., 2012). To decrease run time, we imposed limitations on the maximum data set size and the minimum window size and ran the data set query and windowing steps for both data sets in parallel. The run time could be further diminished by parallelizing the ICP differencing. Differencing a typical data set (~10^8 points) takes ~2–30 min on OpenTopography computer resources at the San Diego Supercomputer Center, depending on a number of factors, including system load.

DISCUSSION

Topographic Differencing Advancements

Here, we address multiple aspects related to efficiently differencing the growing volumes of multitemporal topography data sets. Each year, the number and coverage of airborne lidar data sets increase, and the data set characteristics (i.e., point density) become more varied. To develop on-demand 3-D differencing tools, we addressed two aspects of the workflow that are key to successful

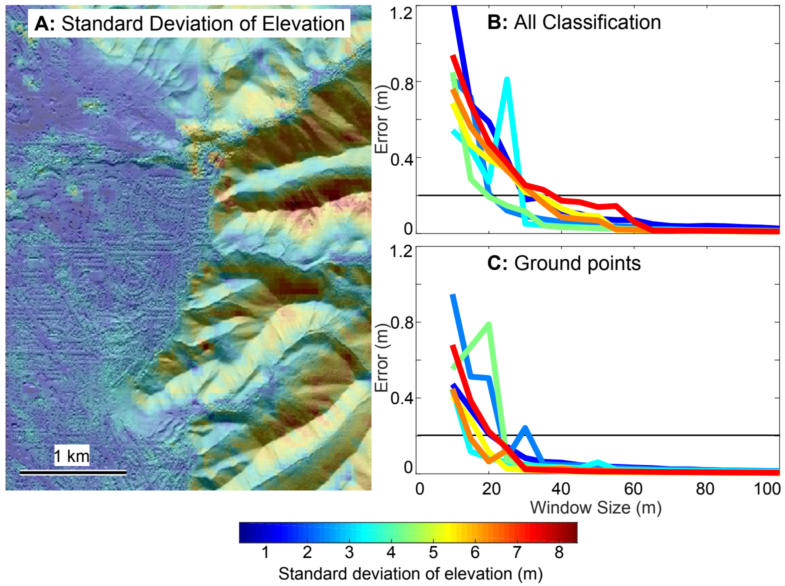

Figure 11. (A) Topographic hillshade from the 2013–2014 State of Utah Wasatch Front airborne light detection and ranging (lidar) data set (Utah, 2014) colored by the standard deviation of elevation over 50 m windows. (B) Mean horizontal displacement error vs. window size for synthetically displaced data for the full data set. Line color—mean standard deviation of elevation; black line—20 cm threshold. (C) Same as B, but for ground-classified points. Location is 40° 44.372′N, 111° 48.425′W.

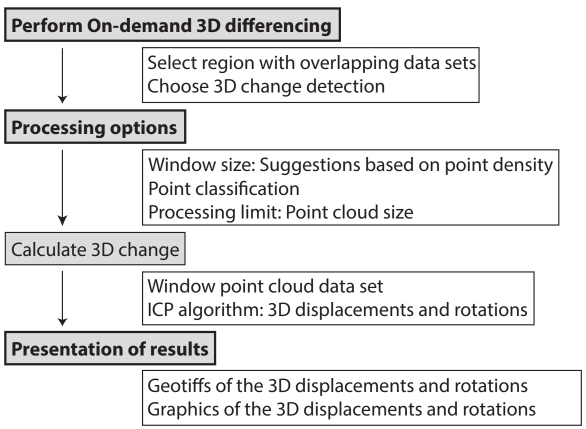

Figure 12. Three-dimensional (3-D) differencing flow chart as implemented in OpenTopography. Bolded text denotes areas of user interaction, including data set selection, processing options, and result visualization. ICP—iterative closest point algorithm.

differencing. (1) Differencing results depend on the selected ICP algorithm: Point-to-plane algorithms are better than point-to-point algorithms and individual algorithms of the same type have varying quality. (2) We incorporated metadata to parametrize the processing: The processing is tailored to point density, which has generally increased over time with the advancement of sensor technology. With these new advances packaged into an easy-to-use tool that is executed on-demand on cloud-based computer resources, students and other geospatial nonexperts can now efficiently perform differencing. More advanced users can experiment and iterate on processing approaches to refine results. The user community has the potential to find new applications for these differencing tools and to incorporate them into initiatives such as hazard response.

Use of OpenTopography's Differencing Tools

Currently, differencing is implemented on over 60 data set pairs in OpenTopography. In the 18 mo following the vertical differencing release, over 1150 successful jobs were run. The 3-D differencing had over 100 successful jobs in the first 6 mo following its release. Usage metrics indicate a diverse user community with many from academia. Others include those from U.S. federal agencies (U.S. Geological Survey, U.S. Forest Service, and National Oceanic and Atmospheric Administration), the Army Corps of Engineers, or industry. The vertical differencing tool was also used in a geographic information systems (GIS) course at Simon Fraser University, Burnaby, British Columbia, Canada. Students related remote-sensing observations to surface processes and considered how processing parameters impacted results. We expect that as we continue to publicize the tool, and the number of overlapping data sets increases, the usage will also grow.

Future Challenges for Differencing

The archive of global and national topography data sets will continue to grow, particularly with ongoing collections including stereo-satellite topography obtained as part of ArcticDEM, satellite lidar, including the Ice, Cloud and Land Elevation Satellite-2 (*ICESat-2*) and Global Ecosystem Dynamics Investigation (GEDI) missions, and national-scale programs such as the U.S. Geologic Survey 3-D Elevation program (3-DEP), among many other projects. A fundamental challenge to enabling differencing on these data sets is to centralize their access such that they can be intercompared.

Differencing will benefit from on-demand techniques that require minimal user input, like those developed here. Performing differencing on high-performance computing resources such as those provided by OpenTopography would enable larger-scale computations relative to local processing. Future methodology to difference hybrid data sets (i.e., optical- and lidar-derived topography) and data sets with greatly varying point spacing (i.e., airborne vs. spaceborne lidar) will expand opportunities. Further, differencing could incorporate color from optical imagery and laser return intensity (Eitel et al., 2016).

CONCLUSION

Vertical and 3-D topographic differencing measures landscape evolution with applications in natural hazards, critical infrastructure monitoring, and basic research in geomorphology and earthquake geodesy. This technology is increasingly in-demand due to the growing multitemporal survey archive. Here, we addressed several challenges that serve as obstacles for many first-time users and explored package algorithms that streamline topographic differencing via OpenTopography. We showed that the 3-D differencing window size (i.e., spatial resolution) depends on the point cloud density, data quality, and vegetation. As additional multitemporal topography data are acquired by spaceborne and airborne platforms, the framework presented here will be adaptable to differencing data sets with varying characteristics.

ACKNOWLEDGMENTS

C. Scott was supported by U.S. National Science Foundation Postdoctoral Fellowship 1625221 and by the School of Earth and Space Exploration at Arizona State University. M. Phan, V. Nandigam, C. Crosby, and J R. Arrowsmith acknowledge grants 1948997, 1948994, and 1948857 from the U.S. National Science Foundation. We thank Steve Delong, Mike Oskin, Andrea Hampel (editor), and three anonymous reviewers for constructive comments on the manuscript. We thank Professor Nick Hedley at Simon Fraser University, Canada, for sharing his experience about using the topographic differencing tool in his class.

We placed the differencing algorithms in several Github repositories: vertical differencing: github.com/OpenTopography/Vertical_Differencing; Python and MATLAB codes for 3-D differencing: github.com/OpenTopography/3D_Differencing. LIBICP (Geiger et al., 2012) was modified to read las files and perform windowed ICP: github.com/OpenTopography/libicp.

REFERENCES CITED

Albino, F., Smets, B., d'Oreye, N., and Kervyn, F., 2015, High-resolution TanDEM-X DEM: An accurate method to estimate lava flow volumes at Nyamulagira Volcano (D.R. Congo): Journal of Geophysical Research–Solid Earth, v. 120, p. 4189–4207, https://doi.org/10.1002/2015JB011988.

Amberg, B., Romdhani, S., and Vetter, T., 2007, Optimal step nonrigid ICP algorithms for surface registration, *in* 2007 IEEE Conference on Computer Vision and Pattern Recognition: Minneapolis, Minnesota, Institute of Electrical and Electronics Engineers (IEEE), p. 1–8, https://doi.org/10.1109/CVPR.2007.383165.

Anders, N., Valente, J., Masselink, R., and Keesstra, S., 2019, Comparing filtering techniques for removing vegetation from UAV-based photogrammetric point clouds: Drones, v. 3, no. 3, p. 61, https://doi.org/10.3390/drones3030061.

Barnhart, W.D., Gold, R.D., Shea, H.N., Peterson, K.E., Briggs, R.W., and Harbor, D.J., 2019, Vertical coseismic offsets derived from high-resolution stereogrammetric DSM differencing: The 2013 Baluchistan, Pakistan, earthquake: Journal of Geophysical Research–Solid Earth, v. 124, p. 6039–6055, https://doi.org/10.1029/2018JB017107.

Beer, A.R., Turowski, J.M., and Kirchner, J.W., 2017, Spatial patterns of erosion in a bedrock gorge: Journal of Geophysical Research–Earth Surface, v. 122, p. 191–214, https://doi.org/10.1002/2016JF003850.

Bellekens, B., Spruyt, V., Berkvens, R., and Maarten, W., 2014, A survey of rigid 3-D pointcloud registration algorithms, *in* Proceedings: AMBIENT 2014: The Fourth International Conference on Ambient Computing, Applications, Services and Technologies: Rome, Italy, p. 8–13.

Besl, P.J., and McKay, N.D., 1992, A method for registration of 3-D shapes: IEEE Transactions on Pattern Analysis and Machine Intelligence, v. 14, p. 239–256, https://doi.org/10.1109/34.121791.

Bevis, M., Hudnut, K., Sanchez, R., Toth, C., Grejner-Brzezinska, D., Kendrick, E., Caccamise, D., Raleigh, D., Zhou, H., Shan, S., Shindle, W., Yong, A., Harvey, J., Borsa, A., Ayoub, F., Shrestha, R., Carter, B., Sartori, M., Phillips, D., and Coloma, F., 2005, The B4 Project: Scanning the San Andreas and San Jacinto fault zones: San Francisco, California, American Geophysical Union, Fall Meeting 2005, abstract H34B–01.

Borsa, A., and Minster, J.-B., 2012, Rapid determination of near-fault earthquake deformation using differential LiDAR: Bulletin of the Seismological Society of America, v. 102, p. 1335–1347, https://doi.org/10.1785/0120110159.

Brasington, J., Langham, J., and Rumsby, B., 2003, Methodological sensitivity of morphometric estimates of coarse fluvial sediment transport: Geomorphology, v. 53, p. 299–316, https://doi.org/10.1016/S0169-555X(02)00320-3.

Brock, J., Sallenger, A., Krabill, W., Swift, R., and Wright, C., 2001, Recognition of fiducial surfaces in lidar surveys of coastal topography: Photogrammetric Engineering and Remote Sensing, v. 67, p. 1245–1258.

Bull, J.M., Miller, H., Gravley, D.M., Costello, D., Hikuroa, D.C.H., and Dix, J.K., 2010, Assessing debris flows using LIDAR differencing: 18 May 2005 Matata event, New Zealand: Geomorphology, v. 124, p. 75–84, https://doi.org/10.1016/j.geomorph.2010.08.011.

Catano, C., 2012, Apopka, Florida: Using LiDAR to Identify Optimal Gopher Tortoise Habitat: OpenTopography, https://doi.org/10.5069/G94M92GW.

Chen, Y., and Medioni, G., 1992, Object modelling by registration of multiple range images: Image and Vision Computing, v. 10, p. 145–155, https://doi.org/10.1016/0262-8856(92)90066-C.

Chiba, T., 2018a, Post-Kumamoto Earthquake (16 April 2016) Rupture LiDAR Scan: OpenTopography, https://doi.org/10.5069/G9SX6B9T.

Chiba, T., 2018b, Pre-Kumamoto Earthquake (16 April 2016) Rupture LiDAR Scan: OpenTopography, https://doi.org/10.5069/G9XP7303.

City of San Diego, 2011, 2005 San Diego Urban Region LiDAR: OpenTopography, https://doi.org/10.5069/G9XW4GQ0.

Clark, K.J., Nissen, E.K., Howarth, J.D., Hamling, I.J., Mountjoy, J.J., Ries, W.F., Jones, K., Goldstien, S., Cochran, U.A., Villamor, P., Hreinsdóttir, S., Litchfield, N.J., Mueller, C., Berryman, K.R., and Strong, D.T., 2017, Highly variable coastal deformation in the 2016 MW 7.8 Kaikōura earthquake reflects rupture complexity along a transpressional plate boundary: Earth and Planetary Science Letters, v. 474, p. 334–344, https://doi.org/10.1016/j.epsl.2017.06.048.

DeLong, S.B., Prentice, C.S., Hilley, G.E., and Ebert, Y., 2012, Multitemporal ALSM change detection, sediment delivery, and process mapping at an active earthflow: Earth Surface Processes and Landforms, v. 37, p. 262–272, https://doi.org/10.1002/esp.2234.

Diablo Canyon Power Plant Long Term Seismic Program (DCPP LTSP), 2013, PG&E Diablo Canyon Power Plant (DCPP): Los Osos, California, Central Coast: OpenTopography, https://doi.org/10.5069/G9J9649Z.

Donnellan, A., Arrowsmith, R., and DeLong, S., 2017, Spatio-temporal mapping of plate boundary faults in California using geodetic imaging: Geosciences, v. 7, p. 15, https://doi.org/10.3390/geosciences7010015.

EarthScope, 2008, EarthScope Northern California LiDAR Project: EarthScope, https://doi.org/10.5069/G9057CV2.

Eitel, J.U.H., Höfle, B., Vierling, L.A., Abellán, A., Asner, G.P., Deems, J.S., Glennie, C.L., Joerg, P.C., LeWinter, A.L., Magney, T.S., Mandlburger, G., Morton, D.C., Müller, J., and Vierling, K.T., 2016, Beyond 3-D: The new spectrum of lidar applications for earth and ecological sciences: Remote Sensing of Environment, v. 186, p. 372–392, https://doi.org/10.1016/j.rse.2016.08.018.

Ekhtari, N., and Glennie, C., 2017, High-resolution mapping of near-field deformation with airborne Earth observation data,

a comparison study: IEEE Transactions on Geoscience and Remote Sensing, v. 56, p. 1–17, https://doi.org/10.1109/TGRS.2017.2765601.
GDAL/OGR contributors, 2019, GDAL/OGR Geospatial Data Abstraction Software Library: Open Source Geospatial Foundation, https://gdal.org (last accessed 15 October 2020).
Geiger, A., Lenz, P., and Urtasun, R., 2012, Are we ready for autonomous driving? The KITTI vision benchmark suite, *in* 2012 IEEE Conference on Computer Vision and Pattern Recognition: Providence, Rhode Island, Institute of Electrical and Electronics Engineers (IEEE), p. 3354–3361, https://doi.org/10.1109/CVPR.2012.6248074.
Glennie, C., 2007, Rigorous 3-D error analysis of kinematic scanning LIDAR systems: Journal of Applied Geodesy, v. 1, p. 147–157, https://doi.org/10.1515/jag.2007.017.
Glennie, C.L., Hinojosa-Corona, A., Nissen, E., Kusari, A., Oskin, M.E., Arrowsmith, J R., and Borsa, A., 2014, Optimization of legacy lidar data sets for measuring near-field earthquake displacements: Geophysical Research Letters, v. 41, p. 3494–3501, https://doi.org/10.1002/2014GL059919.
Goulden, T., and Hopkinson, C., 2010, The forward propagation of integrated system component errors within airborne Lidar data: Photogrammetric Engineering and Remote Sensing, v. 76, p. 589–601, https://doi.org/10.14358/PERS.76.5.589.
Greater Wellington Regional Council (GWRC), 2017, Wellington, New Zealand 2013: OpenTopography, https://doi.org/10.5069/G9CV4FPT.
Haddad, D.E., 2010, Granite Dells, AZ: OpenTopography, https://doi.org/10.5069/G92Z13FN.
Howell, A., Nissen, E., Stahl, T., Clark, K., Kearse, J., Van Dissen, R., Villamor, P., Langridge, R.M., and Jones, K., 2020, 3-D surface displacements during the 2016 M_W: Journal of Geophysical Research–Solid Earth, v. 125, e2019JB018739, https://doi.org/10.1029/2019JB018739.
Hu, Y., 2003, Automated Extraction of Digital Terrain Models, Roads and Buildings Using Airborne LiDAR Data [Ph.D. thesis]: Calgary, Alberta, Canada, Department of Geomatics Engineering, The University of Calgary, 222 p.
Idaho LiDAR Consortium (ILC), 2012, Idaho LiDAR Consortium (ILC): Moscow Mountain: OpenTopography, https://doi.org/10.5069/G9G15XS0.
IndianaMap, 2012, 2011–2013 Indiana Statewide LiDAR: OpenTopography, https://doi.org/10.5069/G9959FHZ.
Isenburg, M., Liu, Y., Snoeyink, J., and Thirion, T., 2006, Generating raster DEM from mass points via TIN streaming, *in* Raubal, M., Miller, H.J., Frank, A.U., and Goodchild , M.F., eds., GIScience'06 Conference Proceedings: Berlin, Heidelberg, Springer-Verlag, p. 186–198, https://doi.org/10.1007/11863939.
Izumida, A., Uchiyama, S., and Sugai, T., 2017, Application of UAV-SfM photogrammetry and aerial lidar to a disastrous flood: Repeated topographic measurement of a newly formed crevasse splay of the Kinu River, central Japan: Natural Hazards and Earth System Sciences, v. 17, p. 1505–1519, https://doi.org/10.5194/nhess-17-1505-2017.
James, M.R., and Robson, S., 2014, Mitigating systematic error in topographic models derived from UAV and ground-based image networks: Earth Surface Processes and Landforms, v. 39, p. 1413–1420, https://doi.org/10.1002/esp.3609.
James, M.R., Robson, S., d'Oleire-Oltmanns, S., and Niethammer, U., 2017, Optimising UAV topographic surveys processed with structure-from-motion: Ground control quality, quantity and bundle adjustment: Geomorphology, v. 280, p. 51–66, https://doi.org/10.1016/j.geomorph.2016.11.021.
Krajewski, W., 2012, 2008 Iowa River Flood LiDAR, Iowa City, and the Clear Creek Watershed: OpenTopography, https://doi.org/10.5069/G90Z715W.
Krishnan, S., Crosby, C., Nandigam, V., Phan, M., Cowart, C., Baru, C., and Arrowsmith, R., 2011, OpenTopography: A services oriented architecture for community access to LIDAR topography, *in* Proceedings of the 2nd International Conference on Computing for Geospatial Research & Applications (COM.Geo '11): Washington, D.C., ACM Press, p. 1–8, https://doi.org/10.1145/1999320.1999327.
Kumar, P., 2016, IML Critical Zone Observatory, Clear Creek Aug 2014 LiDAR Survey: OpenTopography, https://doi.org/10.5069/G9RF5S0N.
Lague, D., Brodu, N., and Leroux, J., 2013, Accurate 3-D comparison of complex topography with terrestrial laser scanner: Application to the Rangitikei canyon (N-Z): ISPRS Journal of Photogrammetry and Remote Sensing, v. 82, p. 10–26, https://doi.org/10.1016/j.isprsjprs.2013.04.009.
Langridge, R.M., Ries, W.F., Farrier, T., Barth, N.C., Khajavi, N., and De Pascale, G.P., 2014, Developing sub 5-m LiDAR DEMs for forested sections of the Alpine and Hope faults, South Island, New Zealand: Implications for structural interpretations: Journal of Structural Geology, v. 64, p. 53–66, https://doi.org/10.1016/j.jsg.2013.11.007.
Lee, H., 2017, Slumgullion Landslide, Colorado: OpenTopography, https://doi.org/10.5069/G91834KD.
Leprince, S., Barbot, S., Ayoub, F., and Avouac, J.-P., 2007, Automatic and precise orthorectification, coregistration, and subpixel correlation of satellite images, application to ground deformation measurements: IEEE Transactions on Geoscience and Remote Sensing, v. 45, p. 1529–1558, https://doi.org/10.1109/TGRS.2006.888937.
Leyland, J., Hackney, C.R., Darby, S.E., Parsons, D.R., Best, J.L., Nicholas, A.P., Aalto, R., and Lague, D., 2017, Extreme flood-driven fluvial bank erosion and sediment loads: Direct process measurements using integrated mobile laser scanning (MLS) and hydro-acoustic techniques: Earth Surface Processes and Landforms, v. 42, p. 334–346, https://doi.org/10.1002/esp.4078.
Low, K., 2004, Linear Least-Squares Optimization for Point-to-Plane ICP Surface Registration: Department of Computer Science, University of North Carolina at Chapel Hill, Technical Report TR04–004, 3 p., https://www.comp.nus.edu.sg/~lowkl/publications/lowk_point-to- plane_icp_techrep.pdf.
Lucieer, A., de Jong, S.M., and Turner, D., 2014, Mapping landslide displacements using Structure from Motion (SfM) and image correlation of multi-temporal UAV photography: Progress in Physical Geography, v. 38, p. 97–116, https://doi.org/10.1177/0309133313515293.
Men, H., Gebre, B., and Pochiraju, K., 2011, Color point cloud registration with 4D ICP algorithm, *in* 2011 IEEE International Conference on Robotics and Automation: Shanghai, China, Institute of Electrical and Electronics Engineers (IEEE), p. 1511–1516, https://doi.org/10.1109/ICRA.2011.5980407.
Milliner, C., Dolan, J.F., Hollingsworth, J., Leprince, S., Ayoub, F., and Sammis, C.G., 2015, Quantifying near-field and off-fault deformation patterns of the 1992 M_w 7.3 Landers earthquake: Geochemistry Geophysics Geosystems, v. 16, p. 1577–1598, https://doi.org/10.1002/2014GC005693.
National Aeronautics and Space Administration (NASA), 2005, West Rainier Seismic Zone, WA: OpenTopography, https://doi.org/10.5069/G9CC0XMC.
National Institute of Advanced Industrial Science and Technology, 2016, Active Fault Database of Japan: National Institute of Advanced Industrial Science and Technology, https://gbank.gsj.jp/activefault/index_e_gmap.html (last accessed 15 October 2020).
Nissen, E., Krishnan, A.K., Arrowsmith, J R., and Saripalli, S., 2012, Three-dimensional surface displacements and rotations from differencing pre- and post-earthquake LiDAR point clouds: Geophysical Research Letters, v. 39, L16301, https://doi.org/10.1029/2012GL052460.
Nissen, E., Maruyama, T., Arrowsmith, J R., Elliott, J.R., Krishnan, A.K., Oskin, M.E., and Saripalli, S., 2014, Coseismic fault zone deformation revealed with differential lidar: Examples from Japanese M_w ~7 intraplate earthquakes: Earth and Planetary Science Letters, v. 405, p. 244–256, https://doi.org/10.1016/j.epsl.2014.08.031.
Okyay, U., Telling, J., Glennie, C.L., and Dietrich, W.E., 2019, Airborne lidar change detection: An overview of earth sciences applications: Earth-Science Reviews, v. 198, 102929, https://doi.org/10.1016/j.earscirev.2019.102929.
Oskin, M.E., Arrowsmith, J R., Hinojosa, A., and Fletcher, J.M., 2010, El Mayor–Cucupah Earthquake (4 April 2010) Rupture LiDAR Scan: OpenTopography, http://opentopo.sdsc.edu/lidarDataset?opentopoID=OTLAS.122010.32611.1.
Oskin, M.E., Arrowsmith, J R., Hinojosa Corona, A., Elliott, A.J., Fletcher, J.M., Fielding, E.J., Gold, P.O., Gonzalez Garcia, J.J., Hudnut, K.W., Liu-Zeng, J., and Teran, O.J., 2012, Near-field deformation from the El Mayor–Cucapah earthquake revealed by differential LiDAR: Science, v. 335, p. 702–705, https://doi.org/10.1126/science.1213778.
PG&E Diablo Canyon Power Plant (DCPP), 2011, Los Osos, CA Central Coast: OpenTopography, https://doi.org/10.5069/G9J9649Z.
Passalacqua, P., Belmont, P., Staley, D.M., Simley, J.D., Arrowsmith, J R., Bode, C.A., Crosby, C., DeLong, S.B., Glenn, N.F., Kelly, S.A., Lague, D., Sangireddy, H., Schaffrath, K., Tarboton, D.G., Wasklewicz, T., and Wheaton, J.M., 2015, Analyzing high resolution topography for advancing the understanding of mass and energy transfer through landscapes: A review: Earth-Science Reviews, v. 148, p. 174–193, https://doi.org/10.1016/j.earscirev.2015.05.012.
PDAL Contributors, 2018, PDAL Point Data Abstraction Library: PDAL, https://doi.org/10.5281/zenodo.2556738.
Prentice, C.S., Crosby, C.J., Whitehill, C.S., Arrowsmith, J R., Furlong, K.P., and Phillips, D.A., 2009, Illuminating Northern California's active faults: Eos (Washington, D.C.), v. 90, p. 55, https://doi.org/10.1029/2009EO070002.
Rusinkiewicz, S., and Levoy, M., 2001, Efficient variants of the ICP algorithm, *in* Proceedings of the Third International Conference on 3D Digital Imaging and Modeling: Quebec City, Quebec, Canada, Institute of Electrical and Electronics Engineers (IEEE), p. 145–152, https://doi.org/10.1109/IM.2001.924423.
Santa Catalina Mountains CZO, 2012a, Jemez River Basin Snow-Off LiDAR Survey: OpenTopography, https://doi.org/10.5069/G9RB72JV.

Santa Catalina Mountains CZO, 2012b, Jemez River Basin Snow-On LiDAR Survey: OpenTopography, https://doi.org/10.5069/G9W37T86.
Schaer, P., Skaloud, J., Landtwing, S., and Legat, K., 2007, Accuracy estimation for laser point cloud including scanning geometry, *in* Vettore, A., and El-Sheimy, N., eds., Proceedings, The 5th International Symposium on Mobile Mapping Technology: Padua, Italy, 8 p., https://www.isprs.org/proceedings/XXXVI/5-C55/papers/schaer_philipp.pdf.
Scott, C., Champenois, J., Klinger, Y., Nissen, E., Maruyama, T., Chiba, T., and Arrowsmith, R., 2019, 2016 M7 Kumamoto, Japan, earthquake slip field derived from a joint inversion of differential lidar topography, optical correlation, and InSAR surface displacements: Geophysical Research Letters, v. 46, no. 12, p. 6341–6351, https://doi.org/10.1029/2019GL082202.
Scott, C., Bunds, M., Shirzaei, M., and Toke, N., 2020, Creep along the Central San Andreas fault from surface fractures, topographic differencing, and InSAR: Journal of Geophysical Research–Solid Earth, v. 125, no. 10, e2020JB019762, https://doi.org/10.1029/2020JB019762.
Scott, C.P., Arrowsmith, J R., Nissen, E., Lajoie, L., Maruyama, T., and Chiba, T., 2018a, The *M*: Journal of Geophysical Research–Solid Earth, v. 123, no. 7, p. 6138–6155, https://doi.org/10.1029/2018JB015581.
Scott, C.P., Scott, T., Lao-Davila, D.A., Clarke, A.B., Arrowsmith, JR., and Lynch, D., 2018b, Photogrammetric Model of the Tecolote Volcano, Sonora, Mexico: OpenTopography, https://doi.org/10.5069/G9028PFR.
San Diego Regional Climate Collaborative (SDRCC), 2018, 2016 Solana Beach, California, Bluff Characterization Survey: OpenTopography, https://doi.org/10.5069/G9HM56JB.
Shean, D.E., Alexandrov, O., Moratto, Z.M., Smith, B.E., Joughin, I.R., Porter, C., and Morin, P., 2016, An automated, open-source pipeline for mass production of digital elevation models (DEMs) from very-high-resolution commercial stereo satellite imagery: ISPRS Journal of Photogrammetry and Remote Sensing, v. 116, p. 101–117, https://doi.org/10.1016/j.isprsjprs.2016.03.012.
Smith, T., Rheinwalt, A., and Bookhagen, B., 2019, Determining the optimal grid resolution for topographic analysis on an airborne lidar dataset: Earth Surface Dynamics, v. 7, p. 475–489, https://doi.org/10.5194/esurf-7-475-2019.
Stock, G., 2012, Yosemite, CA: El Portal, Mariposa Grove, Yosemite Canyon & Tuolumne Meadows: OpenTopography, https://doi.org/10.5069/G9GQ6VP3.
Streutker, D.R., Glenn, N.F., and Shrestha, R., 2011, A slope-based method for matching elevation surfaces: Photogrammetric Engineering and Remote Sensing, v. 77, p. 743–750, https://doi.org/10.14358/PERS.77.7.743.
Susquehanna Shale Hills CZO, 2013a, Susquehanna Shale Hills Critical Zone Observatory, Leaf-Off Survey: OpenTopography, https://doi.org/10.5069/G9VM496T.
Susquehanna Shale Hills CZO, 2013b, Susquehanna Shale Hills Critical Zone Observatory, Leaf-On Survey: OpenTopography, https://doi.org/10.5069/G96W980G.
Toth, C., Brzezinska, D., Csanyi, N., Paska, E., and Yastikli, N., 2007, LiDAR mapping supporting earthquake research of the San Andreas fault: Proceedings of the ASPRS 2007 Annual Conference: Tampa, Florida, American Society for Photogrammetry and Remote Sensing, p. 1–11.
U.S. Forest Service (USFS), 2013, Tahoe National Forest Lidar: OpenTopography, https://doi.org/10.5069/G9ZS2TF2.
U.S. Geological Survey (USGS), 2013, Missisquoi Watershed LiDAR: OpenTopography, https://doi.org/10.5069/G9ST7MR9.
Utah, 2014, State of Utah Acquired LiDAR Data—Wasatch Front: OpenTopography, https://doi.org/10.5069/G9TH8JNQ.
Valentine, G., 2012, Lunar Crater Volcanic Field, Central Nevada: OpenTopography, http://opentopo.sdsc.edu/lidarDataset?opentopoID=OTLAS.022015.26911.1.
Wagner, W., Lague, D., Mohrig, D., Passalacqua, P., Shaw, J., and Moffett, K., 2017, Elevation change and stability on a prograding delta: Geophysical Research Letters, v. 44, no. 4, p. 1786–1794, https://doi.org/10.1002/2016GL072070.
Wedmore, L.N.J., Gregory, L.C., McCaffrey, K.J.W., Goodall, H., and Walters, R.J., 2019, Partitioned off-fault deformation in the 2016 Norcia earthquake captured by differential terrestrial laser scanning: Geophysical Research Letters, v. 46, p. 3199–3205, https://doi.org/10.1029/2018GL080858.
Wheaton, J.M., Brasington, J., Darby, S.E., and Sear, D.A., 2009, Accounting for uncertainty in DEMs from repeat topographic surveys: Improved sediment budgets: Earth Surface Processes and Landforms, v. 35, no. 2, p. 136–156, https://doi.org/10.1002/esp.1886.
Williams, R., and Weaver, C., 2012, New Madrid Seismic Zone: OpenTopography, https://doi.org/10.5069/G94F1NND.
Zimmer, V., 2011, Yosemite National Park, California: Rockfall Studies: OpenTopography, https://doi.org/10.5069/G9D798B8.